

The grain boundary mobility tensor

Kongtao Chen^a, Jian Han^{a,b}, Xiaoqing Pan^c, and David J. Srolovitz^{a,b,1} 

^aDepartment of Materials Science and Engineering, University of Pennsylvania, Philadelphia, PA 19104; ^bDepartment of Materials Science and Engineering, City University of Hong Kong, Kowloon, Hong Kong SAR, China; and ^cDepartment of Materials Science and Engineering, University of California, Irvine, CA 92697

Edited by John W. Hutchinson, Harvard University, Cambridge, MA, and approved January 24, 2020 (received for review November 20, 2019)

The grain-boundary (GB) mobility relates the GB velocity to the driving force. While the GB velocity is normally associated with motion of the GB normal to the GB plane, there is often a tangential motion of one grain with respect to the other across a GB; i.e., the GB velocity is a vector. GB motion can be driven by a jump in chemical potential across a GB or by shear applied parallel to the GB plane; the driving force has three components. Hence, the GB mobility must be a tensor (the off-diagonal components indicate shear coupling). Performing molecular dynamics (MD) simulations on a symmetric-tilt GB in copper, we demonstrate that all six components of the GB mobility tensor are nonzero (the mobility tensor is symmetric, as required by Onsager). We demonstrate that some of these mobility components increase with temperature, while, surprisingly, others decrease. We develop a disconnection dynamics-based statistical model that suggests that GB mobilities follow an Arrhenius relation with respect to temperature T below a critical temperature T_c and decrease as $1/T$ above it. T_c is related to the operative disconnection mode(s) and its (their) energetics. For any GB, which disconnection modes dominate depends on the nature of the driving force and the mobility component of interest. Finally, we examine the impact of the generalization of the mobility for applications in classical capillarity-driven grain growth. We demonstrate that stress generation during GB migration (shear coupling) necessarily slows grain growth and reduces GB mobility in polycrystals.

materials science | thermodynamics | grain growth | grain boundary | molecular dynamics

The most important dynamical property for the evolution of polycrystalline microstructures (e.g., grain growth, recrystallization) is the grain-boundary (GB) mobility. Normally, the GB mobility is defined (1) as the ratio of the GB velocity v to the thermodynamic driving force (per area) F in the limit of infinitesimal driving force, $M = \lim_{F \rightarrow 0} v/F$. GB mobility has been measured in many different metals [e.g., Zn (2), Pb (3), Al (4), Au (5, 6), Cu (7), Fe-Si (8, 9), and Bi (10)] and ceramics [e.g., alumina (11)] and as a function of several variables (e.g., temperature, bicrystallography, and solute concentration) in bicrystal experiments with different types of driving forces [e.g., stress (2), curvature (4–9), and magnetic field (10)], as summarized in ref. 12. More recently, molecular dynamics (MD) simulations have been employed to study GB mobilities in bicrystals as a function of many of the same variables (13–22) and driving forces (13, 15) [as well as driving forces only accessible in simulations (16)]. Olmsted and coworkers (17, 20) systematically studied the mobility of 388 GBs (different macroscopic, bicrystallographic degrees of freedom) in Ni as a function of temperature. GB migration may also be driven by the application of a shear across the GB plane. Shear coupling has been reported in experiments for both metals [e.g., Al (23–31) and Zn (2, 32)] and ceramics [e.g., cubic zirconia (33)] and in a wide range of MD simulations (34–44). The importance of shear coupling in microstructure evolution is illustrated in experimental observations of stress-assisted grain growth in nanocrystalline metals (27, 30).

Recent studies (42–45) suggest that, because of shear coupling, GB mobility depends on the origin of the driving force for

GB migration (stress versus jumps in chemical potential across a GB). This dependence contradicts the widely accepted notion that GB mobility is an intrinsic GB property (independent of the source of the driving force). However, if the GB mobility does depend on the nature of the driving force, the notion of a GB mobility should be expanded. The shear-coupling factor (ratio of GB sliding and migration rates) also depends on the nature of the driving force (44). Hence, GB motion is associated with three orthogonal displacements (and velocities): GB migration (perpendicular to the GB plane) and translations of one grain with respect to the other (in two directions tangent to the GB plane). Accordingly, there are three generalized forces (per unit area) associated with these motions (variations of the free energy with respect to three displacements). Assuming that the displacements associated with the GB motion are overdamped (an excellent approximation since GB velocities are small compared with all speeds of sound), the proportionality constant between the velocity and force vectors should therefore be a 3×3 mobility tensor, \mathbf{M} . If we establish a coordinate system such that the GB normal is parallel to the \mathbf{e}_1 axis, then M_{11} is the traditional GB (migration) mobility, M_{1j} ($j \neq 1$) components describe shear coupling, and M_{ij} ($i, j \neq 1$) describe GB sliding. Since M_{ij}/M_{11} is often not small, ignoring these non-traditional mobility tensor components (i.e., replacing \mathbf{M} with the scalar $M_{GB} = M_{11}$) can be inappropriate. Also note that the individual components of \mathbf{M} may have different temperature dependences.

Here, we employ MD simulations to examine the individual components of the GB mobility tensor \mathbf{M} and their temperature

Significance

Defects and microstructures have a profound impact on material strength and ductility. Microstructure engineering can enhance/trade-off between these properties. One of the key parameters that dictates microstructure evolution is grain-boundary mobility. We demonstrate the fundamental nature of the mobility, reconciling a wide range of observations in a consistent model. We argue that the mobility is, in general, a tensor (classically, it is a scalar) and determine all of its components. We do this by combining molecular-dynamics simulations and the development of a statistical mechanics-based disconnection (line defects in grain boundaries) model. The tensor nature of the mobility explains which grain-boundary characteristics are materials properties and which are not and demonstrates that stress generation always slows grain growth.

Author contributions: K.C., J.H., X.P., and D.J.S. designed research; K.C., J.H., X.P., and D.J.S. performed research; K.C. contributed new analytic tools; K.C. and J.H. analyzed data; and K.C., J.H., X.P., and D.J.S. wrote the paper.

The authors declare no competing interest.

This article is a PNAS Direct Submission.

Published under the PNAS license.

¹To whom correspondence may be addressed. Email: srol@cityu.edu.hk.

This article contains supporting information online at <https://www.pnas.org/lookup/suppl/doi:10.1073/pnas.1920504117/-DCSupplemental>.

First published February 18, 2020.

dependences for a $\Sigma 7$ [111] (12 $\bar{3}$) GB in face-centered cubic (FCC) copper. We focus on this relatively simple, low- Σ symmetric-tilt GB as an example to demonstrate the main effects/principles (additional MD data, not reported here, suggest that the same conclusions apply broadly). We then develop a general statistical disconnection-based analytical model to understand the temperature dependence of the GB mobility tensor \mathbf{M} .

Generalized GB Kinetics

Consider the bicrystal schematic in Fig. 1, where the GB separates grains A and B. The normal displacement of the GB (i.e., the GB migration distance) is u_1 in the x_1 direction. The displacements of grain A with respect to grain B along two orthogonal directions in the GB plane (x_2 and x_3) are u_2 and u_3 , respectively. Thus, we define a generalized displacement $\mathbf{u} = (u_1, u_2, u_3)$ with a corresponding generalized velocity $\mathbf{v} = \dot{\mathbf{u}}$. The generalized driving force conjugate to the generalized velocity is $\mathbf{F} = -\partial G / \partial \mathbf{u}$, where G is the free energy per area of the GB. The first component of \mathbf{F} is $F_1 = -\partial G / \partial u_1 = \psi$, which is the jump of chemical potential (free-energy density) across the GB. The second and third components of \mathbf{F} are $F_2 = \sigma_{12} \equiv \tau_2$ and $F_3 = \sigma_{13} \equiv \tau_3$, which are shear stresses along the x_2 and x_3 directions in the GB plane. The GB mobility tensor, relating \mathbf{v} and \mathbf{F} , i.e.,

$$\mathbf{v} = \mathbf{M}\mathbf{F}, \quad [1]$$

is a second-rank tensor; more explicitly,

$$\begin{pmatrix} v_1 \\ v_2 \\ v_3 \end{pmatrix} = \begin{pmatrix} M_{11} & M_{12} & M_{13} \\ M_{21} & M_{22} & M_{23} \\ M_{31} & M_{32} & M_{33} \end{pmatrix} \begin{pmatrix} \psi \\ \tau_2 \\ \tau_3 \end{pmatrix}. \quad [2]$$

Since GB kinetics are overdamped, GB motion is consistent with the maximum energy-dissipation rate, and, as required by the Onsager relation (46), the GB mobility tensor \mathbf{M} should be symmetric and positive definite (see below).

The shear-coupling factor (the ratio of the shear velocity to the GB migration velocity) has two components $\beta_k = v_k / v_1$ corresponding to orthogonal shear directions. This factor can be obtained by measuring v_1 and v_k under an applied shear stress τ_k ; according to Eq. 2, such a factor is $\beta_k = M_{kk} / M_{1k}$. β_k can also be determined by measuring v_1 and v_k when GB migration is driven by a jump in the chemical potential across the GB ψ

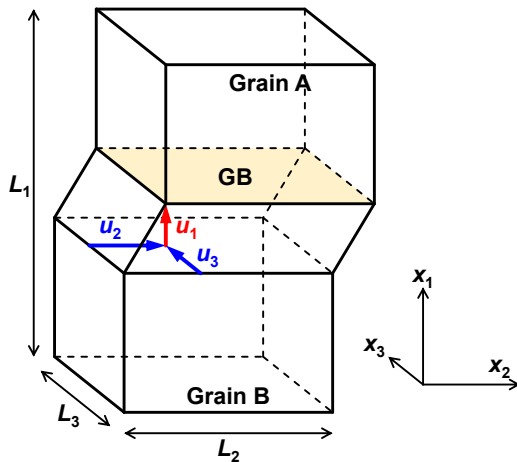


Fig. 1. Bicrystal simulation cell with a symmetric-tilt GB (shaded yellow). The tilt axis is parallel to x_3 , and the GB plane is nominally x_2 - x_3 . The cell is periodic in the x_2 and x_3 directions, and a thin, rigid perfect crystal layer is added to the top and bottom surfaces, which may displace freely.

(e.g., a synthetic driving force such as often employed in MD simulations or associated with capillarity); the factor measured in this way is $\beta_k = M_{1k} / M_{11}$. Coupling factors β_k measured in these two manners are naturally different (44) (*SI Appendix*).

Simulation Methods

We performed MD simulations using the Large-scale Atomic/Molecular Massively Parallel Simulator (47) and a copper embedded-atom-method potential (48) for several different GBs (44). While these simulations (44) show qualitatively similar results, we focus on one particular GB in this paper; i.e., the $\Sigma 7$ [111] (12 $\bar{3}$) symmetric-tilt GB. In these simulations, the tilt axis is parallel to the x_3 direction, and the cell dimensions are $L_1 \sim 100$ nm, L_2 and $L_3 \sim 5$ nm.

We construct GBs by fixing the misorientation of the two grains and minimizing the energy with respect to atomic coordinates and the relative translations of the upper grain relative to the lower grain. We then rescale all atomic coordinates in accordance with the temperature-appropriate lattice constant prior to beginning the MD simulations. Before applying a driving force, we equilibrate the bicrystal system at the temperature of interest for 0.2 ns. In the simulations of stress-driven GB migration, we apply a constant shear stress τ_2 or τ_3 by imposing forces on the top and bottom surfaces of F_2 or F_3 . Additional MD simulations are performed in which GB migration is driven by a jump in the chemical potential ψ ; i.e., an additional energy density $\pm \psi/2$ was added to the atoms in grains A and B, respectively [i.e., a synthetic driving force (16)]. Much larger driving forces were employed to drive GB motion by using applied shear stresses as compared with chemical potential jumps in order to obtain reliable mobility measurements (as seen below, the mobilities obtained for small and large driving forces are consistent). All simulations were run for 7 ns at temperatures in the 600 to 1,300 K range at a fixed number of atoms and temperature (Nosé-Hoover thermostat on all but the fixed atoms). The GB position is defined as the x_1 position where the layer-averaged centro-symmetry parameter (49) is maximum (50). The GB migration velocity is the normal velocity of the mean GB plane. The “error” bars in the GB mobility data depict the values obtained from two identical simulations. All data are contained in the main text and *SI Appendix*.

Simulation Results

Fig. 2 shows the temperature dependence of each of the GB mobility components M_{ij} . The magnitudes of these components can vary by several orders; $M_{11} > M_{1i} > M_{22} > M_{33}$. The temperature dependences of these GB mobility components also differ widely. The components which involve the displacement along the tilt axis (M_{31} , M_{32} , and M_{33}) increase rapidly with increasing temperature (Fig. 2 C, E, and F), while the other components (M_{11} , M_{12} , and M_{22}) decrease with increasing temperature (Fig. 2 A, B, and D).

The observation that the diagonal components M_{11} and M_{22} decrease with increasing temperature seems counterintuitive. But, such situations are, in fact, not unusual; in the MD dataset of 388 distinct GBs, refs. 17 and 20 reported such behavior for many GBs (they call this antithermal behavior). The origin of this surprising temperature dependence of several GB mobility components is discussed below.

Examination of Fig. 2 D–F clearly demonstrates that $M_{12} = M_{21}$, $M_{13} = M_{31}$, and $M_{23} = M_{32}$, as required by the Onsager reciprocal relation (46). Coupling does not only exist between GB migration and shear, but also between shears in different directions; i.e., a shear stress in one direction may produce shear displacement along the orthogonal direction, i.e., in general, $M_{23} \neq 0$. Note that in the symmetric-tilt GB example which we focus on in this report, M_{23} is small compared with the other mobility components.

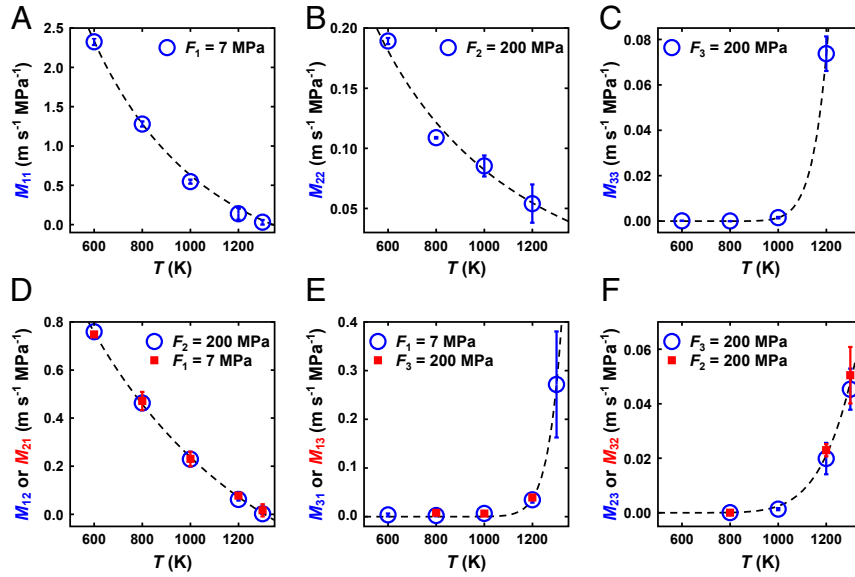


Fig. 2. Temperature dependences of the GB mobility components M_{11} (A), M_{22} (B), M_{33} (C), M_{12} (D), M_{13} (E), and M_{23} (F) (error bars indicate the range of the simulation results). The data points represent the MD results, and the dashed lines are fits of these data to Eq. 5 for a single disconnection mode. For the off-diagonal components of M_{ij} ($i \neq j$), two sets of data points (blue circles and red squares) are shown corresponding to M_{ij} and M_{ji} ; the Onsager relation suggests that these two sets of data are equivalent.

Statistical Disconnection Model

GB motion is accomplished through the glide of line defects (i.e., disconnections) along the GB (45); such a disconnection mechanism has been directly supported by the in situ experimental observation of GB migration in polycrystals by Legros and coworkers (28, 29, 31). Disconnections are constrained to lie within the GB and are characterized by a Burgers vector \mathbf{b} (dislocation character) and a step height h (step character); both of these are translation vectors of the displacement-shift complete lattice (45, 51). For each GB with a particular bicrystallography, there are multiple disconnection modes (\mathbf{b}_m, h_m) (45) (the subscript denotes one of the disconnection modes allowed by the bicrystallography).

Disconnections may be introduced into GBs via homogeneous or heterogeneous nucleation and/or by the decomposition of lattice dislocations. In this discussion, we focus on homogeneous nucleation since, as in phase transformations, heterogeneities often simply rescale the homogeneous nucleation energies. Since disconnection formation and migration may be driven by different types of driving force which couple to the disconnection (\mathbf{b}_m, h_m), the disconnection dipole formation energy depends on the disconnection mode. Following earlier discussions of disconnection formation/nucleation (43–45), we can write the disconnection formation barrier as

$$E^* = Q - W \equiv (A b^2 + B |h| + C) L - \mathbf{H} \cdot \mathbf{F} L^2 / 2, \quad [3]$$

where Q is the formation barrier without a driving force, W is the work done by the driving force, $\mathbf{H} \equiv (h, b_2, b_3)$, and $L = L_2 = L_3$. The constants may be estimated (45) as $A = -2\mu [(1 - \nu \cos^2 \alpha) / 4\pi(1 - \nu)] \ln \sin(\pi r_0 / L)$ and $B = 2\gamma$, where γ is the step energy, μ is the shear modulus, ν is the Poisson's ratio, α is the angle between the Burgers vector and the disconnection line direction, and r_0 is the disconnection core size. A describes the energy required to form a dislocation pair and separate it to a distance of half the periodic unit cell $L/2$ (45), and B describes the energy required to form a pair of steps (43–45). C represents the disconnection migration barrier which depends on the GB structure and bonding character; this is dominated by core-level phenomena and may

be determined via calculations on the atomic scale (52). We emphasize that, in our approach, we view a flat GB as reference configuration, and curvature is directly represented by a distribution of step/disconnection (pairs) along the reference GB. While a macroscopically curved GB is appropriately viewed as flat on the scale of MD simulations (except for nano-grained microstructures), we still capture this macro-curvature driving force as a jump of chemical potential (i.e., ψ as a component of \mathbf{F}); this is consistent with the classical Gibbs–Thomson effect, where GB curvature induces a pressure driving force on a GB—driving force and chemical-potential jump are simply two equivalent approaches for describing the thermodynamics of GB curvature-induced GB migration.

Since the disconnection formation barrier (Eq. 3) depends on both \mathbf{b} and h , disconnections of different modes have different formation rates. We implicitly assume that the GB velocity is disconnection-formation-controlled (i.e., the disconnection-formation barrier is large compared with the migration barrier) and describe the temperature dependence of the disconnection-formation rates based upon Boltzmann statistics (43, 44) [this is not always a good assumption (52)]. Hence, the GB velocity is obtained by superimposing contributions from different disconnection modes, weighted by their Boltzmann factors:

$$\begin{aligned} \mathbf{v} &= 2f_0 \sum_m \mathbf{H}^{(m)} e^{-Q^{(m)}/k_B T} \sinh \left(\frac{\mathbf{H}^{(m)} \cdot \mathbf{F} L^2}{2k_B T} \right) \\ &\approx \left(\frac{f_0 L^2}{k_B T} \sum_m \mathbf{H}^{(m)} \otimes \mathbf{H}^{(m)} e^{-Q^{(m)}/k_B T} \right) \mathbf{F}, \end{aligned} \quad [4]$$

where f_0 is the attempt frequency, the superscript m denotes the m^{th} disconnection mode, and the expression in the second line of Eq. 4 is an expansion to leading order in $\mathbf{F} L^2 / T$. Therefore, the GB mobility tensor is

$$\mathbf{M} = \frac{f_0 L^2}{k_B T} \sum_m \mathbf{H}^{(m)} \otimes \mathbf{H}^{(m)} e^{-Q^{(m)}/k_B T}. \quad [5]$$

Table 1. Activation energy $Q^{(m)}$ and preexponential $c_{ij}^{(m)} \equiv f_0 L^2 H_i^{(m)} H_j^{(m)} / k_B$ for the m^{th} mode for the mobility component M_{ij} , obtained by fitting Eq. 5 to the data in Fig. 2

| | M_{11} | M_{12} | M_{13} | M_{22} | M_{23} | M_{33} |
|-------------------------|----------|----------|----------|----------|----------|----------|
| $\ln(c_{ij}^{(1)}/c_0)$ | 7.5 | 6.2 | 31 | 4.7 | 15 | 25 |
| $Q^{(1)}$ (eV) | ~ 0 | ~ 0 | 2.8 | ~ 0 | 1.2 | 2.1 |
| $\ln(c_{ij}^{(2)}/c_0)$ | 8.8 | 8.3 | — | 5.9 | — | — |
| $Q^{(2)}$ (eV) | 0.2 | 0.2 | — | 0.2 | — | — |

The fit was performed assuming a single-mode expression for M_{i3} ($i = 1, 2, 3$) and a two-mode expression for M_{ij} ($i, j = 1, 2$). The preexponential normalization is $c_0 = 1 \text{ K m s}^{-1} \text{ MPa}^{-1}$. The symbol — in the last two rows indicate that a single-mode model was sufficient (no two-mode fitting was performed).

Eq. 5 guarantees that $\mathbf{M} = \mathbf{M}^T$; the determinant $|\mathbf{M}| > 0$; the diagonal components M_{11} , M_{22} , and M_{33} are each positive; and, generally, $M_{ij} \neq 0$. We also note that because of the temperature-dependent prefactor and the summation over modes, M_{ij} is, in general, non-Arrhenius. If only one mode is active, M_{ij} will reach maximum at $T = T_c \equiv Q^{(1)}/k_B$. For $T < T_c$, M_{ij} will be nearly Arrhenius, while for $T > T_c$, the temperature dependence of M_{ij} is dominated by the prefactor $1/T$. This suggests that M_{ij} may decrease with increasing temperature for $T > T_c$.

Since the $[111]$ tilt axis is a close-packed direction in our material (FCC copper), the modes with Burgers vector \mathbf{b} parallel to the tilt axis (x_3) tend to have much larger values of $|\mathbf{b}|$ and, thus, larger Q (Eq. 3) than the modes with \mathbf{b} perpendicular to the tilt axis (x_2). The large difference in Q between the shears in the directions parallel and perpendicular to the tilt axis makes the investigated temperature range (600 to 1,300 K) smaller than T_c for the former and larger than T_c for the latter. This results in qualitatively different temperature dependences of the mobility components M_{3i} ($i = 1, 2, 3$) and M_{jk} ($j, k = 1, 2$). For M_{3i} (shearing in x_3), $T < T_c$ such that $M_{3i}(T)$ is nearly Arrhenius, in qualitative agreement with the MD results (Fig. 2 C, E, and F). For M_{jk} (shearing in x_1 or x_2), $T > T_c$ such that $M_{jk}(T)$ scales approximately as $1/T$, in qualitative agreement with the MD results (Fig. 2 A, B, and D).

The dashed lines in Fig. 2 show fits to the MD data using a single-mode expression (i.e., the first term in Eq. 5) for M_{i3} ($i = 1, 2, 3$) and a two-mode expression (i.e., the first two terms in Eq. 5) for M_{ij} ($i, j = 1, 2$). The parameters obtained by fitting are listed in Table 1. We find that the mobility components which involve sliding along the tilt axis—i.e., M_{i3} ($i = 1, 2, 3$)—are associated with large activation energies (i.e., $Q^{(1)} \sim 2 \text{ eV}$ in Table 1) in comparison with the activation energies of the other mobility components. This implies that the temperature dependence of these components is dominated by the exponential factor in Eq. 5 (i.e., Arrhenius), and these are well-fitted by the single-mode expression (Fig. 2 C, E, and F). However, for the other mobility components—i.e., M_{ij} ($i, j = 1, 2$)—the activation energy of the first mode is negligible (i.e., $Q^{(1)} \sim 0 \text{ eV}$ in Table 1), such that the temperature dependence is dominated by the $1/T$ prefactor in Eq. 5. For these components, a second mode is required to capture the high-temperature behavior. The activation energy for the second mode is, of course, larger than that of the first mode (i.e., $Q^{(2)} > Q^{(1)}$ for M_{11} , M_{12} , and M_{22} in Table 1).

Discussion

The classical kinetic equation for describing capillarity-driven GB migration is $v_{\perp} = m\psi = m\gamma\kappa$, where γ is the GB energy, and κ is the mean curvature of the GB plane. This description naturally led to a description of the growth of individual

n -sided grains in a two-dimensional (2D) polycrystal [i.e., the von Neumann–Mullins relation (53, 54)]: $\dot{R} = mg\gamma/R$, where R is the grain size and $g = n/6 - 1$ is a factor accounting for grain topology, and we approximated the rate of change of the area of a grain as $R\dot{R}$. Integration leads to one of the classic laws for grain growth: $R^2 - R_0^2 = 2mg\gamma t$, where R_0 is the initial grain size. If we incorporate the tensor character of the mobility, what are the consequences for grain growth?

For the case of the growth/shrinking of a grain in a 2D polycrystal, Eq. 1 can be simplified as

$$\begin{pmatrix} \dot{R} \\ -\dot{\tau}R/\mu \end{pmatrix} = \begin{pmatrix} M_{11} & M_{12} \\ M_{12} & M_{22} \end{pmatrix} \begin{pmatrix} g\gamma/R \\ \tau \end{pmatrix}. \quad [6]$$

$-\dot{\tau}R/\mu$ is the shear across the GB assuming a linear elastic constitutive relation (43). The numerical results are shown in Fig. 3. The numerical values of the terms in the mobility tensor are those extracted from the MD simulations. As expected, 12-sided grains grow, while four-sided grains shrink. At late times, R^2 is a linear function of t , and grain growth is parabolic. However, at early times, R^2 is not a linear function, and grain growth is not parabolic (Fig. 3A). Fig. 3B shows that the grain growth is accompanied by the development of internal stress; for growing grains, this slowly decays with increasing grain size, while for shrinking grains, it diverges as the grain size tends to zero.

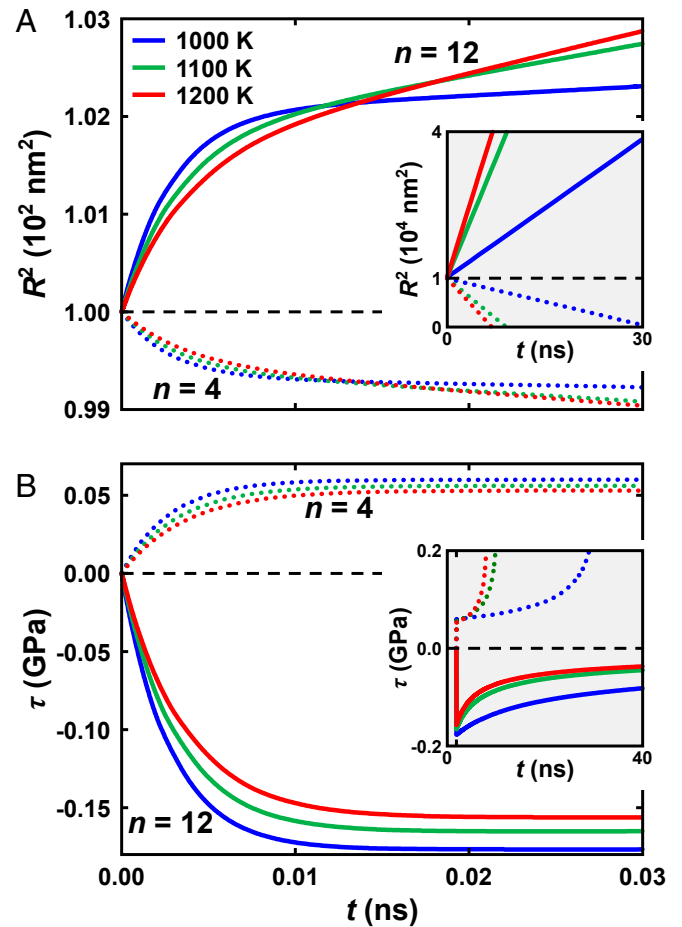


Fig. 3. Numerical results for square of the mean grain size R^2 vs. time t (A) and the shear stress τ vs. time t (B) at 1,000 K (blue), 1,100 K (green), and 1,200 K (red). The solid and dotted lines are for the case of $n = 12$ and 4, respectively (n is the number of edges of a grain in a 2D microstructure). A and B, Insets show the time evolutions for much longer times.

If GB migration and shear are not coupled—i.e., $M_{12} = 0$ —then $R^2 - R_0^2 = 2M_{11}g\gamma t$, and, obviously, no stress develops; this is classical grain growth.

Eq. 6 shows that as $R \rightarrow \infty$, $R^2 - R_0^2 = 2\tilde{m}g\gamma t$, where the effective mobility $\tilde{m} = |\mathbf{M}|/M_{22} = M_{11} - M_{12}^2/M_{22}$. Since \mathbf{M} is positive definite, \tilde{m} is necessarily positive. Also, since $\tilde{m} < M_{11}$, we see that the development of GB migration-induced internal stresses always inhibit grain growth/shrinkage; the apparent GB mobility measured in polycrystals will be smaller than that measured in bicrystals. We also note that \tilde{m} does not necessarily increase with increasing temperature (so-called “thermal” GB migration in refs. 17 and 20). While in the large set of GBs examined by MD (17, 20), thermal GB behavior was more common than antithermal behavior, we note that both possibilities exist here, depending on the relative magnitudes of dM_{11}/dT and $d(M_{12}^2/M_{22})/dT$. While the relationship of \tilde{m} vs. T tends to be increasingly thermal with increasing T (shear coupling is less effective at higher T), there have been experimental observations of antithermal behavior in grain growth at low temperature (55).

While this analysis focused on 2D grain growth (the topological nature of the von Neumann–Mullins result makes this case simple), extensions to higher dimension are straightforward (56) (SI Appendix).

Conclusion

Since GB migration and GB sliding are, in general, coupled, we have extended the notion of the GB velocity-driving force

relation applied throughout the field to account for both this coupling and the interrelation between the different types of GB motion (migration and sliding). The natural extension is from a scalar velocity-mobility-driving-force relation to one in which the velocity and forces may be thought of as vectors and the mobility as a second rank tensor. The kinetic equation suggests the definition of a GB mobility tensor, \mathbf{M} . The diagonal components of \mathbf{M} correspond to the conventional GB mobility and GB sliding coefficient (or the inverse of a GB viscosity). The off-diagonal components of \mathbf{M} reflect coupling between GB migration and GB sliding. We determined the full GB mobility tensor and its temperature dependence for a $\Sigma 7$ [111] ($12\bar{3}$) symmetric-tilt GB in copper via MD simulations. Surprisingly, we found that some components of \mathbf{M} increase with temperature, while others decrease. We were able to explain this temperature dependence as well as several general properties of the mobility tensor based upon analysis of a disconnection model. These results were then applied to analyze the effect of shear coupling on grain growth. In particular, we showed that the effective GB migration mobility will be smaller than that expected based upon bicrystal experiments as a result of stress generation during grain growth in polycrystalline systems.

ACKNOWLEDGMENTS. This research was sponsored by Army Research Office Grant W911NF-19-1-0263. The views and conclusions contained in this document are those of the authors and should not be interpreted as representing the official policies, either expressed or implied, of the Army Research Office or the US government. The US government is authorized to reproduce and distribute reprints for government purposes notwithstanding any copyright notation herein.

1. D. Turnbull, Theory of grain boundary migration rates. *JOM* **3**, 661–665 (1951).
2. C. H. Li, E. H. Edwards, J. Washburn, E. R. Parker, Stress-induced movement of crystal boundaries. *Acta Metall.* **1**, 223–229 (1953).
3. J. W. Rutter, K. T. Aust, Migration of $\{100\}$ tilt grain boundaries in high purity lead. *Acta Metall.* **13**, 181–186 (1965).
4. H. Hu, B. B. Rath, “Influence of solutes on the mobility of tilt boundaries” in *The Nature and Behavior of Grain Boundaries*, H. Hu, Ed. (Springer, New York, NY, 1972), pp. 405–435.
5. W. Grünwald, F. Haessner, Thermisch aktivierte Korngrenzenwanderung in gewalzten Goldnickelkristallen unter dem Einfluss gelöster Fremdatome. *Acta Metall.* **18**, 217–224 (1970).
6. D. A. Molodov, U. Czubayko, G. Gottstein, L. S. Shvindlerman, Mobility of $\{111\}$ tilt grain boundaries in the vicinity of the special misorientation $\Sigma=7$ in bicrystals of pure aluminium. *Scripta Metall. Mater.* **32**, 529–534 (1995).
7. R. Viswanathan, C. L. Bauer, Kinetics of grain boundary migration in copper bicrystals with $\{001\}$ rotation axes. *Acta Metall.* **21**, 1099–1109 (1973).
8. P. Lejček, V. Paidar, J. Adánek, S. Kadečková, Grain boundary migration in $\Sigma=5$ bicrystals of an Fe-3%Si alloy. *Interface Sci.* **1**, 187–199 (1994).
9. M. Furtkamp, G. Gottstein, D. A. Molodov, V. N. Semenov, L. S. Shvindlerman, Grain boundary migration in Fe-3.5% Si bicrystals with $\{001\}$ tilt boundaries. *Acta Mater.* **46**, 4103–4110 (1998).
10. D. A. Molodov, G. Gottstein, F. Heringhaus, L. S. Shvindlerman, True absolute grain boundary mobility: Motion of specific planar boundaries in bi-bicrystals under magnetic driving forces. *Acta Mater.* **46**, 5627–5632 (1998).
11. J. D. Powers, A. M. Glaeser, Grain boundary migration in ceramics. *Interface Sci.* **6**, 23–39 (1998).
12. G. Gottstein, L. S. Shvindlerman, *Grain Boundary Migration in Metals* (Taylor & Francis, Abingdon, UK, 2009).
13. M. Upmanny, D. J. Srolovitz, L. S. Shvindlerman, G. Gottstein, Misorientation dependence of intrinsic grain boundary mobility: Simulation and experiment. *Acta Mater.* **47**, 3901–3914 (1999).
14. H. Zhang, M. I. Mendelev, D. J. Srolovitz, Computer simulation of the elastically driven migration of a flat grain boundary. *Acta Mater.* **52**, 2569–2576 (2004).
15. H. Zhang, M. I. Mendelev, D. J. Srolovitz, Mobility of $\Sigma 5$ tilt grain boundaries: Inclination dependence. *Scripta Mater.* **52**, 1193–1198 (2005).
16. K. G. F. Janssens *et al.*, Computing the mobility of grain boundaries. *Nat. Mater.* **5**, 124–127 (2006).
17. D. L. Olmsted, E. A. Holm, S. M. Foiles, Survey of computed grain boundary properties in face-centered cubic metals—II: Grain boundary mobility. *Acta Mater.* **57**, 3704–3713 (2009).
18. J. Zhou, V. Mohles, Towards realistic molecular dynamics simulations of grain boundary mobility. *Acta Mater.* **59**, 5997–6006 (2011).
19. H. Song, J. J. Hoyt, A molecular dynamics simulation study of the velocities, mobility and activation energy of an austenite-ferrite interface in pure Fe. *Acta Mater.* **60**, 4328–4335 (2012).
20. E. R. Homer, E. A. Holm, S. M. Foiles, D. L. Olmsted, Trends in grain boundary mobility: Survey of motion mechanisms. *JOM* **66**, 114–120 (2014).
21. M. J. Rahman, H. S. Zurob, J. J. Hoyt, A comprehensive molecular dynamics study of low-angle grain boundary mobility in a pure aluminum system. *Acta Mater.* **74**, 39–48 (2014).
22. J. L. Priedeman, D. L. Olmsted, E. R. Homer, The role of crystallography and the mechanisms associated with migration of incoherent twin grain boundaries. *Acta Mater.* **131**, 553–563 (2017).
23. H. Fukutomi, T. Iseki, T. Endo, T. Kamijo, Sliding behavior of coincidence grain boundaries deviating from ideal symmetric tilt relationship. *Acta Metall. Mater.* **39**, 1445–1448 (1991).
24. M. Winning, G. Gottstein, L. S. Shvindlerman, Stress induced grain boundary motion. *Acta Mater.* **49**, 211–219 (2001).
25. M. Winning, G. Gottstein, L. S. Shvindlerman, On the mechanisms of grain boundary migration. *Acta Mater.* **50**, 353–363 (2002).
26. M. Winning, A. D. Rollett, Transition between low and high angle grain boundaries. *Acta Mater.* **53**, 2901–2907 (2005).
27. D. S. Gianola *et al.*, Stress-assisted discontinuous grain growth and its effect on the deformation behavior of nanocrystalline aluminum thin films. *Acta Mater.* **54**, 2253–2263 (2006).
28. M. Legros, D. S. Gianola, K. J. Hemker, In situ TEM observations of fast grain-boundary motion in stressed nanocrystalline aluminum films. *Acta Mater.* **56**, 3380–3393 (2008).
29. F. Mompou, D. Caillard, M. Legros, Grain boundary shear-migration coupling—I. In situ TEM straining experiments in Al polycrystals. *Acta Mater.* **57**, 2198–2209 (2009).
30. T. J. Rupert, D. S. Gianola, Y. Gan, K. J. Hemker, Experimental observations of stress-driven grain boundary migration. *Science* **326**, 1686–1690 (2009).
31. A. Rajabzadeh, M. Legros, N. Combe, F. Mompou, D. A. Molodov, Evidence of grain boundary dislocation step motion associated to shear-coupled grain boundary migration. *Phil. Mag.* **93**, 1299–1316 (2013).
32. D. W. Bainbridge, H. L. Choh, E. H. Edwards, Recent observations on the motion of small angle dislocation boundaries. *Acta Metall.* **2**, 322–333 (1954).
33. H. Yoshida, K. Yokoyama, N. Shibata, Y. Ikuhara, T. Sakuma, High-temperature grain boundary sliding behavior and grain boundary energy in cubic zirconia bicrystals. *Acta Mater.* **52**, 2349–2357 (2004).
34. L.-Q. Chen, G. Kalonji, Finite temperature structure and properties of $\Sigma = 5$ (310) tilt grain boundaries in NaCl a molecular dynamics study. *Philos. Mag.* **A 66**, 11–26 (1992).
35. C. Molteni, G. P. Francis, M. C. Payne, V. Heine, First principles simulation of grain boundary sliding. *Phys. Rev. Lett.* **76**, 1284–1287 (1996).
36. C. Molteni, N. Marzari, M. C. Payne, V. Heine, Sliding mechanisms in aluminum grain boundaries. *Phys. Rev. Lett.* **79**, 869–872 (1997).
37. N. Chandra, P. Dang, Atomistic simulation of grain boundary sliding and migration. *J. Mater. Sci.* **34**, 655–666 (1999).
38. J. C. Hamilton, S. M. Foiles, First-principles calculations of grain boundary theoretical shear strength using transition state finding to determine generalized gamma surface cross sections. *Phys. Rev. B* **65**, 064104 (2002).
39. A. J. Haslam *et al.*, Stress-enhanced grain growth in a nanocrystalline material by molecular-dynamics simulation. *Acta Mater.* **51**, 2097–2112 (2003).
40. M. Shiga, W. Shinoda, Stress-assisted grain boundary sliding and migration at finite temperature: A molecular dynamics study. *Phys. Rev. B* **70**, 054102 (2004).

41. F. Sansoz, J. F. Molinari, Mechanical behavior of Σ tilt grain boundaries in nanoscale Cu and Al: A quasicontinuum study. *Acta Mater.* **53**, 1931–1944 (2005).
42. J. W. Cahn, Y. Mishin, A. Suzuki, Coupling grain boundary motion to shear deformation. *Acta Mater.* **54**, 4953–4975 (2006).
43. S. L. Thomas, K. Chen, J. Han, P. K. Purohit, D. J. Srolovitz, Reconciling grain growth and shear-coupled grain boundary migration. *Nat. Commun.* **8**, 1764 (2017).
44. K. Chen, J. Han, S. L. Thomas, D. J. Srolovitz, Grain boundary shear coupling is not a grain boundary property. *Acta Mater.* **167**, 241–247 (2019).
45. J. Han, S. L. Thomas, D. J. Srolovitz, Grain-boundary kinetics: A unified approach. *Prog. Mater. Sci.* **98**, 386–476 (2018).
46. L. Onsager, Reciprocal relations in irreversible processes. I. *Phys. Rev.* **37**, 405–426 (1931).
47. S. Plimpton, Fast parallel algorithms for short-range molecular dynamics. *J. Comput. Phys.* **117**, 1–19 (1995).
48. Y. Mishin, M. J. Mehl, D. A. Papaconstantopoulos, A. F. Voter, J. D. Kress, Structural stability and lattice defects in copper: Ab initio, tight-binding, and embedded-atom calculations. *Phys. Rev. B* **63**, 224106 (2001).
49. A. Stukowski, Visualization and analysis of atomistic simulation data with OVITO—The Open Visualization Tool. *Model. Simulat. Mater. Sci. Eng.* **18**, 015012 (2010).
50. C. L. Kelchner, S. J. Plimpton, J. C. Hamilton, Dislocation nucleation and defect structure during surface indentation. *Phys. Rev. B* **58**, 11085–11088 (1998).
51. A. P. Sutton, R. W. Balluffi, *Interfaces in Crystalline Materials* (Clarendon Press Oxford, UK, 1995).
52. N. Combe, F. Momprou, M. Legros, Disconnections kinks and competing modes in shear-coupled grain boundary migration. *Phys. Rev. B* **93**, 024109 (2016).
53. J. Von Neumann, "Discussion: Shape of metal grains" in *Metal Interfaces*, C. Herring, Ed. (American Society for Metals, Cleveland, OH, 1952), pp. 108–110.
54. W. W. Mullins, Two-dimensional motion of idealized grain boundaries. *J. Appl. Phys.* **27**, 900–904 (1956).
55. W. Rheinheimer, M. J. Hoffmann, Non-Arrhenius behavior of grain growth in strontium titanate: New evidence for a structural transition of grain boundaries. *Scripta Mater.* **101**, 68–71 (2015).
56. R. D. MacPherson, D. J. Srolovitz, The von Neumann relation generalized to coarsening of three-dimensional microstructures. *Nature* **446**, 1053–1055 (2007).